

Highlights

- Neural trajectory in the hippocampus showed greater variations during a WM task compared to EC and amygdala regions.
- The distance of neural trajectory in the hippocampus between encoding and retrieval states were memory-load dependent.
- Hippocampal neural trajectory fluctuated between the encoding and retrieval states in a task-dependent manner
- Hippocampal neural trajectory shifted from encoding to retrieval states during sharp-wave ripple event

Hippocampal neural fluctuation between memory encoding and retrieval in a working memory task in humans: An encoding-to-retrieval shift during sharp-wave ripples

Yusuke Watanabe^{a,*}, Yuji Ikegaya^{b,c,d}, Takufumi Yanagisawa^{a,e}

^a*Institute for Advanced Cocreation studies, Osaka University, 2-2 Yamadaoka, Suita, 565-0871, Osaka, Japan*

^b*Graduate School of Pharmaceutical Sciences, The University of Tokyo, 7-3-1 Hongo, Tokyo, 113-0033, Japan*

^c*Institute for AI and Beyond, The University of Tokyo, 7-3-1 Hongo, Tokyo, 113-0033, Japan*

^d*Center for Information and Neural Networks, National Institute of Information and Communications Technology, 1-4 Yamadaoka, Suita City, 565-0871, Osaka, Japan*

^e*Department of Neurosurgery, Osaka University Graduate School of Medicine, 2-2 Yamadaoka, Osaka, 565-0871, Japan*

Abstract

Working memory (WM) is critical for various cognitive functions, yet the underlying neural mechanisms remain obscure. Although the hippocampus and sharp-wave ripple complexes (SWRs) — transient and synchronous neural bursts in the hippocampus — are recognized for their roles in memory consolidation and retrieval, their relationship with WM tasks is poorly understood. This study hypothesizes that multiunit activity patterns in the human hippocampus, in conjunction with SWRs, exhibit distinct behaviors during WM tasks. To test this hypothesis, we employed a dataset consisting of intracranial electroencephalogram recordings from the medial temporal lobe (MTL) of nine epilepsy patients during an eight-second Sternberg test. Gaussian-process factor analysis was utilized to derive low-dimensional neural representations, or ‘trajectories’, specific to WM tasks within MTL areas. Our findings demonstrate that the hippocampus displays the most significant variations in neural trajectory compared to the entorhinal cortex and amygdala. Moreover, the distance of trajectories between encoding and retrieval phases was memory-load dependent. Notably, the hippocampal trajectory fluctuated between the encoding and retrieval states in a task-dependent manner, with a shift from encoding to retrieval states during SWRs. These observations underscore the hippocampus’s pivotal role in WM tasks and provide novel insights into the functional contributions of the hippocampus to WM demands.

Keywords: working memory, WM, memory load, hippocampus, sharp-wave ripples, SWR, humans

1. Introduction

Working memory (WM) is crucial in everyday life; however, its neural mechanism has yet to be fully elucidated. Specifically, the role of the hippocampus, an essential brain region guiding memory and spatial navigation, has been a topic of ongoing controversy [1] [2] [3] [4] [5] [6] [7] [8] [9]. Understanding the hippocampus’ role in working memory is instrumental in deepening our knowledge of cognitive processes, ultimately aiding in developing cognitive training strategies and interventions.

Among the hippocampal phenomena, a transient and synchronous oscillation called sharp-wave ripple (SWR) [10] is associated with various cognitive functions, including memory replay [11] [12] [13] [14] [15], memory consolidation [16] [17] [18] [19], memory recall [20] [21] [22], and neural plasticity [23] [24]. However, investigations into the effects of SWRs on working memory remain infrequent ([25] and limited to rodent models using navigation tasks, in which the precise timings of memory acquisition and recall are not separated.

Hippocampal neurons may exhibit low-dimensional representations during WM tasks. For instance, the firing patterns of place cells [26] [27] [28] [29] [30] in

*Corresponding author. Tel: +81-6-6879-3652

the hippocampus were found to be embedded within a dynamic, nonlinear 3D hyperbolic geometry while rodent navigating [31]. Furthermore, grid cells in the entorhinal cortex (EC) — the primary gateway to the hippocampus [32] [33] [34] — exhibited toroidal topology during exploration [35]. However, again, these experiments are limited to spatial navigation tasks in rodents so that the temporal resolution of WM tasks is constrained. Moreover, whether these findings are generalized to humans, especially other than navigation tasks, are not investigated yet.

Given these backgrounds, in this study, we investigated the hypothesis that hippocampal neurons exhibit distinct representations in low-dimensional spaces as 'neural trajectory' during WM tasks, with a specific focus on SWR periods. To test this hypothesis, we utilized a dataset of patients performing an eight-second Sternbeug task with high temporal resolution (1 s for fixation, 2 s for encoding, 3 s for maintenance, and 2 s for retrieval) while their intracranial electroencephalography signals (iEEG) in the medial temporal lobe (MTL) were recorded [36]. To explore low-dimensional neural trajectories, we employed Gaussian-process factor analysis (GPFA) based on multiunit activities, a proven tool for the analysis of neural population dynamics [37].

2. Methods

2.1. Dataset

A publicly accessible dataset [36] was employed, in which nine subjects performed a modified Sternberg task that consisted of fixation (1 s), encoding (2 s), maintenance (3 s), and retrieval (2 s) phases [36]. During the encoding phase, participants were presented sets of either four, six, or eight alphabetical letters (set size). Subsequently, they were tasked with ascertaining whether a probe letter presented in the retrieval phase had been displayed (the correct choice for Match IN task) or not (the correct choice for Mismatch OUT task). iEEG signals were recorded at a sampling rate of 32 kHz, within the frequency range of 0.5–5,000 Hz, using depth electrodes implanted in the medial temporal regions. Specifically, electrodes were placed in the left and right hippocampal head (AHL and AHR), hippocampal body (PHL and PHR), entorhinal cortex (ECL and ECR), and amygdala (AL and AR) (Figure 1A and Table 1). Subsequently, iEEG signals were resampled

at a rate of 2 kHz. Correlations were found among the experimental variables such as set size and correct rate (Figure S1). The timings of multiunit spikes were estimated by a spike sorting algorithm [38] by the Combinato package (<https://github.com/jniediek/combinato>) (Figure 1C).

2.2. Calculation of neural trajectories using GPFA

To calculate the neural trajectories (also referred to as factors; Figure 1D) in the hippocampus, EC, and amygdala (Figure 1D), GPFA [37], was employed on the multiunit activity data for each session. GPFA was applied using the elephant package (<https://elephant.readthedocs.io/en/latest/reference/gpfa.html>). The bin size was set as 50 ms, with no overlaps. Each factor was z-normalized across each session. From the trajectories, Euclidean distance from the origin ($O(0,0,0)$) was calculated (Figure 1E).

For every trajectory within a region (*e.g.*, AHL), *geometric medians* were determined by calculating the median coordinates of trajectory during the four phases: (*i.e.*, g_F for fixation, g_E for encoding, g_M for maintenance, and g_R for retrieval phase) (Figure 1D). The optimal dimensionality for GPFA was determined as three via the elbow method utilizing the log-likelihood values using the threefold cross-validation approach (Figure 2B).

2.3. Defining SWR candidates from hippocampal regions

To identify potential SWR events within the hippocampus, we employed a detection method aligned with a consensus in this field [39]. Specifically, local field potential (LFP) signals from a region of interest (ROI), such as AHL, were re-referenced by subtracting a control signal obtained by averaging signals from outside the ROI (*e.g.*, AHR, PHL, PHR, ECL, ECR, AL, and AR) (see Figure 1A). The LFP signals were applied to a ripple-band filter (80–140 Hz) to isolate SWR candidates (SWR⁺ candidates) (see Figure 1B). SWR detection was conducted using a published tool (https://github.com/Eden-Kramer-Lab/ripple_detection) [40], with modifications such as an updated bandpass range of 80–140 Hz for humans from original 150–250 Hz range primarily for rodents.

As control events for SWR^+ candidates, SWR^- candidates were defined by shuffling the timestamps of SWR^+ candidates across all trials from all subjects. Finally, the $\text{SWR}^+/\text{SWR}^-$ candidates were visually inspected (see Figure 1).

2.4. Defining SWRs from putative hippocampal CA1 regions

SWRs were defined from SWR candidates as follows. First, putative CA1 regions were defined as follows. First, $\text{SWR}^+/\text{SWR}^-$ candidates in the hippocampus were embedded into a two-dimensional space based on their superimposed spike counts per unit using UMAP (uniform manifold approximation and projection) [41] in a supervised fashion (Figure 4A). The silhouette score [42], a validation barometer for clustering, was calculated from clustered samples (Table 2). The hippocampal regions with silhouette scores greater than 0.6 on average across sessions 75th percentile) (Figure 4B) were defined as putative CA1 regions, identifying five electrode positions from five patients (Table 3).

As a second step, $\text{SWR}^+/\text{SWR}^-$ candidates in putative CA1 regions were defined as $\text{SWR}^+/\text{SWR}^-$ (no longer candidates). The duration and ripple band peak amplitude of detected SWRs were calculated (Figure 4C & E). $\text{SWR}^+/\text{SWR}^-$ were visually inspected as shown in Figure 1. The duration and ripple band peak amplitudes of detected SWRs were quantified (Figure 4C & E). Each SWR was split into pre-SWR (= event at -800 to -300 ms from SWR center), mid-SWR (= event at -250 to +250 ms from SWR center), and post-SWR (= event at +300 to +800 ms from SWR center).

2.5. Statistical evaluation

The Brunner–Munzel test and the Kruskal–Wallis test were executed using the *scipy* package in Python [43]. A correlational analysis was undertaken through the determination of the rank of the observed correlation coefficient in the associated set-size-shuffled surrogate, using a custom Python script. Additionally, the bootstrap test was carried out by utilizing an internally developed Python script.

3. Results

3.1. iEEG recording and neural trajectory in MTL regions during a Sternberg task

We employed a publicly available dataset [36] for this analysis. This dataset recorded LFP signals (Figure 1A) within the MTL regions (Table 1) during a modified Sternberg task. SWR^+ candidates were identified from LFP signals passed through the ripple band (Figure 1B) within all hippocampal regions (refer to Methods), while SWR^- candidates were designated at identical timestamps of the SWR^+ candidates but shuffling them across different trials (Figure 1). The multiunit spikes (Figure 1C) were included in the dataset, being established using a spike sorting algorithm [38]. Using the 50-ms binned multiunit activity without overlaps, we employed GPFA [37] to determine the neural trajectory (or factors) of the MTL regions by session and region (Figure 1D). Each factor was z-normalized by session and region (for example, session #2 in AHL of subject #1). Subsequently, the Euclidean distance from the origin (O) was calculated (Figure 1E).

3.2. Hippocampal neural trajectory correlated with a WM task

In Figure 2A, the median neural trajectories of 50 trials are depicted as points within the three major factor space. The optimal embedding dimension for the GPFA model was determined to be three using the elbow method (Figure 2B). The trajectory distance from the origin (O) for the hippocampus was larger compared to the EC and amygdala (Figure C & D).¹

Similarly, the distance among geometric medians of the four phases were calculated: *i.e.*, $\|\mathbf{g}_{\text{FGE}}\|$) for the distance between fixation and encoding states. Again, the hippocampus showed larger distances among phases compared to both the EC and amygdala.²

¹Hippocampus: Distance = 1.11 [1.01], median [IQR], $n = 195,681$ timepoints; EC: Distance = 0.94 [1.10], median [IQR], $n = 133,761$ timepoints; Amygdala: Distance = 0.78 [0.88], median [IQR], $n = 165,281$ timepoints.

²Hippocampus: Distance = 0.60 [0.70], median [IQR], $n = 8,772$ combinations; EC: Distance = 0.28 [0.52], median [IQR], $n = 5,017$ combinations ($p < 0.01$; Brunner–Munzel test); Amygdala: Distance = 0.24 [0.42], median [IQR], $n = 7,466$ combinations ($p < 0.01$; Brunner–Munzel test).

3.3. Memory load-dependent neural trajectory distance between the encoding and retrieval states in the hippocampus

Correct rate of trials and set size (the number of alphabetical letters to encode) were negatively correlated (Figure 3A).³ Similarly, response time and set size were positively correlated (Figure 3B).⁴

Set size and the trajectory distance between the encoding and retrieval phases ($\log_{10}||g_{EGR}||$) were positively correlated (Figure 3C).⁵ However, no significant correlations were found between set size and distance among other phase combinations (Figures 3D & S2).

3.4. Detection of hippocampal SWR from putative CA1 regions

Under the aim to improve the precision of recording sites and the detection of SWRs, we identified electrodes in putative CA1 regions of the hippocampus based on observing distinct multiunit spike patterns during SWR events. For each session and hippocampal region, SWR⁺/SWR⁻ candidates were embedded into a two-dimensional space via UMAP (Figure 4A).⁶ We calculated the silhouette score as a measure of clustering quality (Figure 4B & Table 2). Recording sites with an average silhouette score across sessions exceeding 0.6 were designated as putative CA1 regions⁷ (Tables 2 & 3). Consequently, four regions out of the five putative CA1 areas had not been identified as seizure onset zones, while one had been designated (Table 1).

Subsequently, SWR⁺/SWR⁻ candidates within these

putative CA1 regions were labeled SWR⁺ and SWR⁻, respectively⁸ (Table 3). Both SWR⁺ and SWR⁻ exhibited an identical duration⁹ (Figure 4C) due to their definitions, following a log-distribution profile. A marked increase in SWR⁺ incidence was detected during the initial 400 ms from the onset of the retrieval phase¹⁰ (Figure 4D). Additionally, the peak ripple band amplitude for SWR⁺ exceeded that of SWR⁻ and followed a log-normal distribution (Figure 4E).¹¹

3.5. Transient neural trajectory change in the hippocampus during SWR

The distances of trajectory from the origin (*O*) during SWR events in both the encoding and retrieval phases (*i.e.*, eSWR⁺, eSWR⁻, rSWR⁺, and rSWR⁻) were calculated (Figure 5A). Given the pronounced peak in them, we categorized each SWR into three stages: pre-SWR, mid-SWR, and post-SWR. Subsequently, the distances from *O* during these SWR periods are represented as $||\text{pre-eSWR}^+||$, $||\text{mid-eSWR}^+||$, and so on.

$||\text{mid-eSWR}^+||$ ¹² was larger than $||\text{pre-eSWR}^+||$ ¹³ (Figure 5B). Similarly, $||\text{mid-rSWR}^+||$ ¹⁴ was larger than $||\text{pre-rSWR}^+||$.¹⁵

3.6. Visualization of hippocampal neural trajectory during SWR in two-dimensional spaces

Based on our observations of neural trajectory 'jump' during SWR (Figure 5), we visualized the trajectories of pre-, mid-, and post-SWR events during the encoding and retrieval phases (Figure 6), the distance of which was memory-load dependent (Figure 3).

To achieve the visualization in two dimension spaces,

³Correct rate: set size four (0.99 ± 0.11 , mean \pm SD; $n = 333$ trials) vs. set size six (0.93 ± 0.26 ; $n = 278$ trials; $p < 0.001$, Brunner–Munzel test with Bonferroni correction) and set size eight (0.87 ± 0.34 ; $n = 275$ trials; $p < 0.05$; Brunner–Munzel test with Bonferroni correction). Overall, $p < 0.001$ for Kruskal–Wallis test; correlation coefficient = -0.20, $p < 0.001$.

⁴Response time: set size four (1.26 ± 0.45 s; $n = 333$ trials) vs. set size six (1.53 ± 0.91 s; $n = 278$ trials) and set size eight (1.66 ± 0.80 s; $n = 275$ trials). All comparisons $p < 0.001$, Brunner–Munzel test with Bonferroni correction; $p < 0.001$ for Kruskal–Wallis test; correlation coefficient = 0.22, $p < 0.001$.

⁵Correlation between set size and $\log_{10}||g_{EGR}||$: correlation coefficient = 0.05, $p < 0.001$. Specific values: $||g_{EGR}|| = 0.54$ [0.70] for set size four trials, $n = 447$; $||g_{EGR}|| = 0.58$ [0.66] for set size six trials, $n = 381$; $||g_{EGR}|| = 0.61$ [0.63] for set size eight trials, $n = 395$.

⁶For illustrative purposes, consider the AHL in session #1 of subject #1.

⁷The identified regions were: AHL of subject #1, AHR of subject #3, PHL of subject #4, AHL of subject #6, and AHR of subject #9.

⁸Definitions lead to equal counts for both categories: SWR⁺ ($n = 1,170$) and SWR⁻ ($n = 1,170$).

⁹Definitions lead to equal duration for both categories: SWR⁺ (93.0 [65.4] ms) and SWR⁻ (93.0 [65.4] ms).

¹⁰SWR⁺ increased against the bootstrap sample; 95th percentile = 0.42 [Hz]; $p < 0.05$.

¹¹SWR⁺ (3.05 [0.85] SD of baseline, median [IQR]; $n = 1,170$) vs. SWR⁻ (2.37 [0.33] SD of baseline, median [IQR]; $n = 1,170$; $p < 0.001$; Brunner–Munzel test).

¹²1.25 [1.30], median [IQR], $n = 1,281$, in Match IN task; 1.12 [1.35], median [IQR], $n = 1,163$, in Mismatch OUT task

¹³1.08 [1.07], median [IQR], $n = 1,149$, in Match IN task; 0.90 [1.12], median [IQR], $n = 1,088$, in Mismatch OUT task

¹⁴1.32 [1.24], median [IQR], $n = 935$, in Match IN task; 1.15 [1.26], median [IQR], $n = 891$, in Mismatch OUT task

¹⁵1.19 [0.96], median [IQR], $n = 673$, in Match IN task; 0.94 [0.88], median [IQR], $n = 664$, in Mismatch OUT task

the peri-SWR trajectories were aligned linearly by positioning \mathbf{g}_E at the origin (0, 0) and placing \mathbf{g}_R at ($\|\mathbf{g}_E\mathbf{g}_R\|$, 0). These aligned trajectories were rotated around the x axis for visualization purposes. Importantly, distances and angles in the original three-dimensional spaces are preserved in these two-dimensional ones.

The scatter plot in these two-dimensional spaces illustrates characteristic distributions of peri-SWR trajectories based on phases and task types. For instance, longer distance of mid-eSWR⁺, compared to pre-eSWR⁻, from \mathbf{g}_E can be observed (Figure 6B), consistent with our earlier findings (Figure 5).

3.7. Fluctuations of hippocampal neural trajectories between encoding and retrieval states

Subsequently, we checked trajectory directions based on $\overrightarrow{\mathbf{g}_E\mathbf{g}_R}$. SWR directions were defined by neural trajectory at -250 ms and +250 ms from their center (*i.e.*, eSWR⁺).

$\overrightarrow{\mathbf{eSWR}^+} \cdot \overrightarrow{\mathbf{rSWR}^+}$ showed a bias towards +1 in Match IN task (Figure 7A) but towards -1 in Mismatch OUT task (Figure 7B). These tendencies were also observed in $\overrightarrow{\mathbf{eSWR}^-} \cdot \overrightarrow{\mathbf{rSWR}^-}$ (Figure 7C-F).

Moreover, $\overrightarrow{\mathbf{rSWR}^+} \cdot \overrightarrow{\mathbf{g}_E\mathbf{g}_R}$ showed a biphasic distribution in Match IN task (Figure 7A) in contrast to a monophasic distribution in Mismatch IN task (Figure 7B).

Both in Match IN and Mismatch OUT tasks, by taking the differences between the distribution of $\overrightarrow{\mathbf{rSWR}^+} \cdot \overrightarrow{\mathbf{g}_E\mathbf{g}_R}$ (Figure 7A & B) and that of $\overrightarrow{\mathbf{rSWR}^-} \cdot \overrightarrow{\mathbf{g}_E\mathbf{g}_R}$ (Figure 7C & D), the effect of SWR was revealed as a shift from \mathbf{g}_E to \mathbf{g}_R (Figure 7E & F).

4. Discussion

This study hypothesized that hippocampal multiunit activity exhibits distinct representations, or trajectories, in low-dimensional spaces during a WM task in humans, particularly during SWR periods. First, we projected the multiunit activity from MTL regions during a Sternberg task onto three-dimensional spaces by GPFA (Figure 1D-E and Figure 2A). The distance of trajectory among WM phases was larger in the hippocampus than the EC and amygdala (Figure 2E), showing more dynamical neural activity in the hippocampus during the WM task. Additionally, the distance trajectory between

the encoding and retrieval phases in the hippocampus ($\|\mathbf{g}_F\mathbf{g}_E\|$) was positively correlated with memory load (Figure 3C & D), indicating it as a reflection of WM processing. Furthermore, the trajectory exhibited a transient 'jump' during SWRs (Figure 5). Finally, the hippocampal neural trajectory fluctuated between encoding and retrieval states, with a shift from encoding to retrieval during SWR events (Figure 7). In sum, these results demonstrated the hippocampal neural behavior in a WM task in humans.

First, we found that the distance of the trajectory among the four phases of the WM task ($\|\mathbf{g}_F\mathbf{g}_E\|$, $\|\mathbf{g}_F\mathbf{g}_M\|$, $\|\mathbf{g}_F\mathbf{g}_R\|$, $\|\mathbf{g}_E\mathbf{g}_M\|$, $\|\mathbf{g}_E\mathbf{g}_R\|$, and $\|\mathbf{g}_M\mathbf{g}_R\|$) was longer in the hippocampus compared to the EC and amygdala, even considering the distance from O ($\|\mathbf{g}_F\|$, $\|\mathbf{g}_E\|$, $\|\mathbf{g}_M\|$, and $\|\mathbf{g}_R\|$) in those regions (Figure 2C-E). These results indicate hippocampal participation in the WM task, which is partially supported by previous findings of hippocampal persistent firing in the maintenance phase [3] [4] [5] [6]. However, by applying GPFA to multiunit activity during the 1-s level resolution of WM task, we revealed that the trajectory in low dimensional space displayed memory-load dependent distance between the encoding and retrieval phase, or $\|\mathbf{g}_E\mathbf{g}_R\|$ (Figure 3). Overall, these results provide evidence that the hippocampus is linked to WM.

The validity of confining our analysis to putative CA1 regions (Figure 4) is supported by several factors. First, this targeted approach stems from well-established observations that SWRs are time-locked to synchronous spike bursts of interneurons and pyramidal neurons [44] [45] [46] [47], possibly around 50 μm radius of the recording site [48]. Additionally, the incidence of detected SWR increased at 0-400 ms from the onset of the retrieval phase (Figure 4D), which is consistent with previous reports showing increased hippocampal SWR occurrence before spontaneous verbal recall [21] [22]. Moreover, the log-normal distributions of SWR duration and ripple band peak amplitude observed in this study (Figure 4C & E) align with the consensus in this field [39]. Therefore, our approach would have increased precision of SWR detection. One limitation is that the increase in trajectory distance from O during SWR (Figure 5) would have been biased because of the channel selection; however, this possibility is not critical for our major findings.

Interestingly, the trajectory directions in the retrieval

phase oscillated between the encoding and retrieval states (Figure 7C & D). In addition, the balance of such fluctuation was shifted from the encoding to retrieval state during SWR (Figure 7 E & F; red rectangle-dotted line). These results are again consistent with previous reports suggesting SWR's role in memory recall [21] [22]. Therefore, our results will provide new aspects of the hippocampal representations: (i) neural fluctuations between encoding and retrieval states during a WM task and (ii) SWR as a switching representation from encoding to retrieval state.

Moreover, our study reveals WM-task type specific directions of SWR trajectory (Figure 7). To illustrate, $\overrightarrow{\text{eSWR}}$ and $\overrightarrow{\text{rSWR}}$ were closely aligned in Match IN task (Figure 7A; pink dotted line), while they are directed to the adverse direction in Mismatch OUT task (Figure 7B; pink dotted line). These result might be explained by the memory engram theory [49]. Match In task exposed subjects to once-seen letter, while Mismatch OUT task make them encounter with a novel letter. These results suggest that SWR is highly related to working cognitive processess in humans.

In conclusion, our study has demonstrated that hippocampal activity fluctuates between encoding and retrieval states during baseline periods and exhibits a significant transition from the encoding state to the retrieval state during SWRs. These findings suggest the applicability of the two-stage memory formation model [44] to working memory tasks on a timescale of seconds.

References

- [1] W. B. Scoville, B. Milner, LOSS OF RECENT MEMORY AFTER BILATERAL HIPPOCAMPAL LESIONS, *Journal of Neurology, Neurosurgery, and Psychiatry* 20 (1) (1957) 11–21. URL <https://www.ncbi.nlm.nih.gov/pmc/articles/PMC497229/>
- [2] L. R. Squire, The Legacy of Patient H.M. for Neuroscience, *Neuron* 61 (1) (2009) 6–9. doi:10.1016/j.neuron.2008.12.023. URL <https://www.ncbi.nlm.nih.gov/pmc/articles/PMC2649674/>
- [3] E. Boran, T. Fedele, P. Klaver, P. Hilfiker, L. Stieglitz, T. Grunwald, J. Sarthein, Persistent hippocampal neural firing and hippocampal-cortical coupling predict verbal working memory load, *Science Advances* 5 (3) (2019) eaav3687. doi:10.1126/sciadv.aav3687. URL <https://www.science.org/doi/10.1126/sciadv.aav3687>
- [4] J. Kamiński, S. Sullivan, J. M. Chung, I. B. Ross, A. N. Mamelak, U. Rutishauser, Persistently active neurons in human medial frontal and medial temporal lobe support working memory, *Nature Neuroscience* 20 (4) (2017) 590–601, number: 4 Publisher: Nature Publishing Group. doi:10.1038/nn.4509. URL <https://www.nature.com/articles/nn.4509>
- [5] S. Kornblith, R. Q. Quiroga, C. Koch, I. Fried, F. Mormann, Persistent Single-Neuron Activity during Working Memory in the Human Medial Temporal Lobe, *Current Biology* 27 (7) (2017) 1026–1032, publisher: Elsevier. doi:10.1016/j.cub.2017.02.013. URL [https://www.cell.com/current-biology/abstract/S0960-9822\(17\)30149-5](https://www.cell.com/current-biology/abstract/S0960-9822(17)30149-5)
- [6] M. C. M. Faraut, A. A. Carlson, S. Sullivan, O. Tudusciuc, I. Ross, C. M. Reed, J. M. Chung, A. N. Mamelak, U. Rutishauser, Dataset of human medial temporal lobe single neuron activity during declarative memory encoding and recognition, *Scientific Data* 5 (1) (2018) 180010, number: 1 Publisher: Nature Publishing Group. doi:10.1038/sdata.2018.10. URL <https://www.nature.com/articles/sdata201810>
- [7] A. A. Borders, C. Ranganath, A. P. Yonelinas, The hippocampus supports high-precision binding in visual working memory, *Hippocampus* 32 (3) (2022) 217–230. doi:10.1002/hipo.23401.
- [8] J. Li, D. Cao, S. Yu, X. Xiao, L. Imbach, L. Stieglitz, J. Sarthein, T. Jiang, Functional specialization and interaction in the amygdala-hippocampus circuit during working memory processing, *Nature Communications* 14 (1) (2023) 2921, number: 1 Publisher: Nature Publishing Group. doi:10.1038/s41467-023-38571-w. URL <https://www.nature.com/articles/s41467-023-38571-w>
- [9] V. Dimakopoulos, P. Mégevand, L. H. Stieglitz, L. Imbach, J. Sarthein, Information flows from hippocampus to auditory cortex during replay of verbal working memory items, *eLife* 11 (2022) e78677, publisher: eLife Sciences Publications, Ltd. doi:10.7554/eLife.78677. URL <https://doi.org/10.7554/eLife.78677>
- [10] G. Buzsáki, Hippocampal sharp wave-ripple: A cognitive biomarker for episodic memory and planning, *Hippocampus* 25 (10) (2015) 1073–1188, _eprint: <https://onlinelibrary.wiley.com/doi/pdf/10.1002/hipo.22488>. doi:<https://doi.org/10.1002/hipo.22488>. URL <https://onlinelibrary.wiley.com/doi/abs/10.1002/hipo.22488>
- [11] M. A. Wilson, B. L. McNaughton, Reactivation of hippocampal ensemble memories during sleep, *Science (New York, N.Y.)* 265 (5172) (1994) 676–679. doi:10.1126/science.8036517.
- [12] Z. Nádasdy, H. Hirase, A. Czurkó, J. Csicsvari, G. Buzsáki, Replay and Time Compression of Recurring Spike Sequences in the Hippocampus, *Journal of Neuroscience* 19 (21) (1999) 9497–9507, publisher: Society for Neuroscience Section: ARTICLE. doi:10.1523/JNEUROSCI.19-21-09497.1999. URL <https://www.jneurosci.org/content/19/21/9497>
- [13] A. K. Lee, M. A. Wilson, Memory of sequential experience in the hippocampus during slow wave sleep, *Neuron* 36 (6) (2002)

- 1183–1194. doi:10.1016/s0896-6273(02)01096-6.
- [14] K. Diba, G. Buzsáki, Forward and reverse hippocampal place-cell sequences during ripples, *Nature Neuroscience* 10 (10) (2007) 1241–1242, number: 10 Publisher: Nature Publishing Group. doi:10.1038/nn1961.
URL <https://www.nature.com/articles/nn1961>
- [15] T. J. Davidson, F. Kloosterman, M. A. Wilson, Hippocampal replay of extended experience, *Neuron* 63 (4) (2009) 497–507. doi:10.1016/j.neuron.2009.07.027.
- [16] G. Girardeau, K. Benchenane, S. I. Wiener, G. Buzsáki, M. B. Zugaro, Selective suppression of hippocampal ripples impairs spatial memory, *Nature Neuroscience* 12 (10) (2009) 1222–1223. doi:10.1038/nn.2384.
URL <http://www.nature.com/articles/nn.2384>
- [17] V. Ego-Stengel, M. A. Wilson, Disruption of ripple-associated hippocampal activity during rest impairs spatial learning in the rat, *Hippocampus* 20 (1) (2010) 1–10. doi:10.1002/hipo.20707.
- [18] A. Fernández-Ruiz, A. Oliva, E. Fermino de Oliveira, F. Rocha-Almeida, D. Tingley, G. Buzsáki, Long-duration hippocampal sharp wave ripples improve memory, *Science (New York, N.Y.)* 364 (6445) (2019) 1082–1086. doi:10.1126/science.aax0758.
URL <https://www.ncbi.nlm.nih.gov/pmc/articles/PMC6693581/>
- [19] J. Kim, A. Joshi, L. Frank, K. Ganguly, Cortical–hippocampal coupling during manifold exploration in motor cortex, *Nature* (2022) 1–8 Publisher: Nature Publishing Group. doi:10.1038/s41586-022-05533-z.
URL <https://www.nature.com/articles/s41586-022-05533-z>
- [20] C.-T. Wu, D. Haggerty, C. Kemere, D. Ji, Hippocampal awake replay in fear memory retrieval, *Nature Neuroscience* 20 (4) (2017) 571–580. doi:10.1038/nn.4507.
- [21] Y. Norman, E. M. Yeagle, S. Khuvis, M. Harel, A. D. Mehta, R. Malach, Hippocampal sharp-wave ripples linked to visual episodic recollection in humans, *Science* 365 (6454) (2019) eaax1030. doi:10.1126/science.aax1030.
URL <https://www.sciencemag.org/lookup/doi/10.1126/science.aax1030>
- [22] Y. Norman, O. Raccach, S. Liu, J. Parvizi, R. Malach, Hippocampal ripples and their coordinated dialogue with the default mode network during recent and remote recollection, *Neuron* 109 (17) (2021) 2767–2780.e5, publisher: Elsevier. doi:10.1016/j.neuron.2021.06.020.
URL [https://www.cell.com/neuron/abstract/S0896-6273\(21\)00461-X](https://www.cell.com/neuron/abstract/S0896-6273(21)00461-X)
- [23] C. J. Behrens, L. P. van den Boom, L. de Hoz, A. Friedman, U. Heinemann, Induction of sharp wave–ripple complexes in vitro and reorganization of hippocampal networks, *Nature Neuroscience* 8 (11) (2005) 1560–1567, number: 11 Publisher: Nature Publishing Group. doi:10.1038/nn1571.
URL <https://www.nature.com/articles/nn1571>
- [24] H. Norimoto, K. Makino, M. Gao, Y. Shikano, K. Okamoto, T. Ishikawa, T. Sasaki, H. Hioki, S. Fujisawa, Y. Ikegaya, Hippocampal ripples down-regulate synapses, *Science (New York, N.Y.)* 359 (6383) (2018) 1524–1527. doi:10.1126/science.aao0702.
- [25] S. P. Jadhav, C. Kemere, P. W. German, L. M. Frank, Awake Hippocampal Sharp-Wave Ripples Support Spatial Memory, *Science* 336 (6087) (2012) 1454–1458, publisher: American Association for the Advancement of Science. doi:10.1126/science.1217230.
URL <https://www.science.org/doi/abs/10.1126/science.1217230>
- [26] J. O’Keefe, J. Dostrovsky, The hippocampus as a spatial map: Preliminary evidence from unit activity in the freely-moving rat, *Brain Research* 34 (1971) 171–175, place: Netherlands Publisher: Elsevier Science. doi:10.1016/0006-8993(71)90358-1.
- [27] J. O’Keefe, Place units in the hippocampus of the freely moving rat, *Experimental Neurology* 51 (1) (1976) 78–109. doi:10.1016/0014-4886(76)90055-8.
URL <https://www.sciencedirect.com/science/article/pii/0014488676900558>
- [28] A. D. Ekstrom, M. J. Kahana, J. B. Caplan, T. A. Fields, E. A. Isham, E. L. Newman, I. Fried, Cellular networks underlying human spatial navigation, *Nature* 425 (6954) (2003) 184–188, number: 6954 Publisher: Nature Publishing Group. doi:10.1038/nature01964.
URL <https://www.nature.com/articles/nature01964>
- [29] K. B. Kjelstrup, T. Solstad, V. H. Brun, T. Hafting, S. Leutgeb, M. P. Witter, E. I. Moser, M.-B. Moser, Finite Scale of Spatial Representation in the Hippocampus, *Science* 321 (5885) (2008) 140–143, publisher: American Association for the Advancement of Science. doi:10.1126/science.1157086.
URL <https://www.science.org/doi/abs/10.1126/science.1157086>
- [30] C. D. Harvey, F. Collman, D. A. Dombeck, D. W. Tank, Intracellular dynamics of hippocampal place cells during virtual navigation, *Nature* 461 (7266) (2009) 941–946, number: 7266 Publisher: Nature Publishing Group. doi:10.1038/nature08499.
URL <https://www.nature.com/articles/nature08499>
- [31] H. Zhang, P. D. Rich, A. K. Lee, T. O. Sharpee, Hippocampal spatial representations exhibit a hyperbolic geometry that expands with experience, *Nature Neuroscience* (Dec. 2022). doi:10.1038/s41593-022-01212-4.
URL <https://www.nature.com/articles/s41593-022-01212-4>
- [32] P. A. Naber, F. H. Lopes da Silva, M. P. Witter, Reciprocal connections between the entorhinal cortex and hippocampal fields CA1 and the subiculum are in register with the projections from CA1 to the subiculum, *Hippocampus* 11 (2) (2001) 99–104, eprint: <https://onlinelibrary.wiley.com/doi/pdf/10.1002/hipo.1028>. doi:10.1002/hipo.1028.
URL <https://onlinelibrary.wiley.com/doi/abs/10.1002/hipo.1028>
- [33] N. M. van Strien, N. L. M. Cappaert, M. P. Witter, The anatomy of memory: an interactive overview of the parahippocampal–hippocampal network, *Nature Reviews Neuroscience* 10 (4) (2009) 272–282, number: 4 Publisher: Nature Publishing Group. doi:10.1038/nrn2614.
URL <https://www.nature.com/articles/nrn2614>
- [34] B. A. Strange, M. P. Witter, E. S. Lein, E. I. Moser, Functional organization of the hippocampal longitudinal axis, *Nature Reviews Neuroscience* 15 (10) (2014) 655–669, number: 10 Pub-

- lisher: Nature Publishing Group. doi:10.1038/nrn3785.
URL <https://www.nature.com/articles/nrn3785>
- [35] R. J. Gardner, E. Hermansen, M. Pachitariu, Y. Burak, N. A. Baas, B. A. Dunn, M.-B. Moser, E. I. Moser, Toroidal topology of population activity in grid cells, *Nature* 602 (7895) (2022) 123–128, number: 7895 Publisher: Nature Publishing Group. doi:10.1038/s41586-021-04268-7.
URL <https://www.nature.com/articles/s41586-021-04268-7>
- [36] E. Boran, T. Fedele, A. Steiner, P. Hilfiker, L. Stieglitz, T. Grunwald, J. Sarnthein, Dataset of human medial temporal lobe neurons, scalp and intracranial EEG during a verbal working memory task, *Scientific Data* 7 (1) (2020) 30, number: 1 Publisher: Nature Publishing Group. doi:10.1038/s41597-020-0364-3.
URL <https://www.nature.com/articles/s41597-020-0364-3>
- [37] B. M. Yu, J. P. Cunningham, G. Santhanam, S. I. Ryu, K. V. Shenoy, M. Sahani, Gaussian-Process Factor Analysis for Low-Dimensional Single-Trial Analysis of Neural Population Activity, *Journal of Neurophysiology* 102 (1) (2009) 614–635. doi:10.1152/jn.90941.2008.
URL <https://www.ncbi.nlm.nih.gov/pmc/articles/PMC2712272/>
- [38] J. Niediek, J. Boström, C. E. Elger, F. Mormann, Reliable Analysis of Single-Unit Recordings from the Human Brain under Noisy Conditions: Tracking Neurons over Hours, *PLOS ONE* 11 (12) (2016) e0166598, publisher: Public Library of Science. doi:10.1371/journal.pone.0166598.
URL <https://journals.plos.org/plosone/article?id=10.1371/journal.pone.0166598>
- [39] A. A. Liu, S. Henin, S. Abbaspoor, A. Bragin, E. A. Buffalo, J. S. Farrell, D. J. Foster, L. M. Frank, T. Gedankien, J. Gotman, J. A. Guidera, K. L. Hoffman, J. Jacobs, M. J. Kahana, L. Li, Z. Liao, J. J. Lin, A. Losonczy, R. Malach, M. A. van der Meer, K. McClain, B. L. McNaughton, Y. Norman, A. Navas-Olive, L. M. de la Prida, J. W. Rueckemann, J. J. Sakon, I. Skelin, I. Soltesz, B. P. Staresina, S. A. Weiss, M. A. Wilson, K. A. Zaghloul, M. Zugaro, G. Buzsáki, A consensus statement on detection of hippocampal sharp wave ripples and differentiation from other fast oscillations, *Nature Communications* 13 (1) (2022) 6000, number: 1 Publisher: Nature Publishing Group. doi:10.1038/s41467-022-33536-x.
URL <https://www.nature.com/articles/s41467-022-33536-x>
- [40] K. Kay, M. Sosa, J. E. Chung, M. P. Karlsson, M. C. Larkin, L. M. Frank, A hippocampal network for spatial coding during immobility and sleep, *Nature* 531 (7593) (2016) 185–190. doi:10.1038/nature17144.
- [41] L. McInnes, J. Healy, N. Saul, L. Großberger, UMAP: Uniform Manifold Approximation and Projection, *Journal of Open Source Software* 3 (29) (2018) 861. doi:10.21105/joss.00861.
URL <https://joss.theoj.org/papers/10.21105/joss.00861>
- [42] P. J. Rousseeuw, Silhouettes: A graphical aid to the interpretation and validation of cluster analysis, *Journal of Computational and Applied Mathematics* 20 (1987) 53–65. doi:10.1016/0377-0427(87)90125-7.
URL <https://www.sciencedirect.com/science/article/pii/0377042787901257>
- [43] P. Virtanen, R. Gommers, T. E. Oliphant, M. Haberland, T. Reddy, D. Cournapeau, E. Burovski, P. Peterson, W. Weckesser, J. Bright, S. J. van der Walt, M. Brett, J. Wilson, K. J. Millman, N. Mayorov, A. R. J. Nelson, E. Jones, R. Kern, E. Larson, C. J. Carey, Polat, Y. Feng, E. W. Moore, J. VanderPlas, D. Laxalde, J. Perktold, R. Cimrman, I. Henriksen, E. A. Quintero, C. R. Harris, A. M. Archibald, A. H. Ribeiro, F. Pedregosa, P. van Mulbregt, SciPy 1.0 Contributors, SciPy 1.0: fundamental algorithms for scientific computing in Python, *Nature Methods* 17 (2020) 261–272, aDS Bibcode: 2020NatMe..17..261V. doi:10.1038/s41592-019-0686-2.
URL <https://ui.adsabs.harvard.edu/abs/2020NatMe..17..261V>
- [44] G. Buzsáki, Two-stage model of memory trace formation: a role for "noisy" brain states, *Neuroscience* 31 (3) (1989) 551–570. doi:10.1016/0306-4522(89)90423-5.
- [45] M. L. V. Quyen, A. Bragin, R. Staba, B. Crépon, C. L. Wilson, J. Engel, Cell Type-Specific Firing during Ripple Oscillations in the Hippocampal Formation of Humans, *Journal of Neuroscience* 28 (24) (2008) 6104–6110, publisher: Society for Neuroscience Section: Brief Communications. doi:10.1523/JNEUROSCI.0437-08.2008.
URL <https://www.jneurosci.org/content/28/24/6104>
- [46] S. Royer, B. V. Zemelman, A. Losonczy, J. Kim, F. Chance, J. C. Magee, G. Buzsáki, Control of timing, rate and bursts of hippocampal place cells by dendritic and somatic inhibition, *Nature Neuroscience* 15 (5) (2012) 769–775, number: 5 Publisher: Nature Publishing Group. doi:10.1038/nn.3077.
URL <https://www.nature.com/articles/nn.3077>
- [47] N. Hájos, M. R. Karlócai, B. Németh, I. Ulbert, H. Monyer, G. Szabó, F. Erdélyi, T. F. Freund, A. I. Gulyás, Input-output features of anatomically identified CA3 neurons during hippocampal sharp wave/ripple oscillation in vitro, *The Journal of Neuroscience: The Official Journal of the Society for Neuroscience* 33 (28) (2013) 11677–11691. doi:10.1523/JNEUROSCI.5729-12.2013.
- [48] E. W. Schomburg, C. A. Anastassiou, G. Buzsáki, C. Koch, The Spiking Component of Oscillatory Extracellular Potentials in the Rat Hippocampus, *The Journal of Neuroscience* 32 (34) (2012) 11798–11811. doi:10.1523/JNEUROSCI.0656-12.2012.
URL <https://www.ncbi.nlm.nih.gov/pmc/articles/PMC3459239/>
- [49] X. Liu, S. Ramirez, P. T. Pang, C. B. Puryear, A. Govindarajan, K. Deisseroth, S. Tonegawa, Optogenetic stimulation of a hippocampal engram activates fear memory recall, *Nature* 484 (7394) (2012) 381–385, number: 7394 Publisher: Nature Publishing Group. doi:10.1038/nature11028.
URL <https://www.nature.com/articles/nature11028>

Contributors

Y.W. and T.Y. conceptualized the study; Y.W. performed the data analysis; Y.W. and T.Y. wrote the original draft; and all authors reviewed the final manuscript.

Acknowledgments

This research was funded by a grant from the Exploratory Research for Advanced Technology (JPM-JER1801).

Declaration of Interests

The authors declare that they have no competing interests.

Data and code availability

The data is available on G-Node (<https://doi.org/10.12751/g-node.d76994/>). The source code is available on GitHub (<https://github.com/yanagisawa-lab/hippocampal-neural-fluctuation-during-a-WM-task-in-humans>).

Inclusion and Diversity Statement

We support inclusive, diverse, and equitable conduct of research.

Declaration of Generative AI in Scientific Writing

The authors employed ChatGPT, provided by OpenAI, for enhancing the manuscript's English language quality. After incorporating the suggested improvements, the authors meticulously revised the content. Ultimate responsibility for the final content of this publication rests entirely with the authors.

Tables

		Hipp. head		Hipp. Body		EC		Amy.			
Subject ID	# of										
sessions	AHL	AHR	PHL	PHR	ECL	ECR	AL	AR		SOZ	
#1	4	o	x	o	o	o	x	o	x		AHR, LR
#2	7	o	o	o	o	o	o	o	o		AHR, PHR
#3	3	o	o	o	o	o	o	o	x		AHL, PHL
#4	2	o	o	o	o	o	o	o	o		AHL, AHR, PHL, PHR
#5	3	o	x	x	o	x	x	o	x		DRR
#6	6	o	o	o	o	o	o	o	o		AHL, PHL, ECL, AL
#7	4	o	o	o	o	o	o	o	o		AHR, PHR
#8	5	o	o	o	o	o	o	o	o		ECR
#9	2	o	o	o	o	o	o	o	o		ECR, AR

Table 1 – Electrode positions of the dataset

The electrode positions and the seizure onset zones. Regions marked as "o" were available, but those marked as "x" (*navy*) were not available in the dataset. Abbreviations: AHL, left hippocampal head; AHR, right hippocampal head; PHL, left hippocampal body; PHR, right hippocampal body; ECL, left entorhinal cortex; ECR, right entorhinal cortex; AL, left amygdala; AR, right amygdala, SOZ: seizure onset zone.

	Hipp. head		Hipp. body	
Subject	AHL	AHR	PHL	PHR
#1	0.60 ± 0.14	n.a.	n.a.	0.1 ± 0
#2	0.21 ± 0.16	0.17 ± 0.21	0.18 ± 0.22	0.20 ± 0.15
#3	0.40 ± 0.42	0.83 ± 0.12	n.a.	n.a.
#4	0.10 ± 0.00	0.10 ± 0.00	0.90 ± 0.00	0.10 ± 0.14
#5	n.a.	n.a.	n.a.	n.a.
#6	0.63 ± 0.06	n.a.	n.a.	0.27 ± 0.06
#7	0.10 ± 0.00	0.35 ± 0.35	0.37 ± 0.47	0.10 ± 0.00
#8	0.13 ± 0.10	n.a.	0.28 ± 0.49	n.a.
#9	n.a.	0.85 ± 0.07	0.15 ± 0.07	n.a.

Table 2 – The silhouette score of UMAP clustering between SWR^+ candidates and SWR^- candidates

The silhouette scores (mean ± SD for sessions by subject) of UMAP clustering on SWR^+ candidates and SWR^- candidates (Figure 4A) were based on their underlying multiunit spike patterns (mean values were 0.205 [0.285], median [IQR]; Figure 4B).

	# of sessions	# of trials	ROI	# of SWRs	SWR incidence [Hz]
#1	2	100	AHL	274	0.34
#3	2	97	AHR	325	0.42
#4	2	99	PHL	202	0.26
#6	2	100	AHL	297	0.37
#9	2	97	AHR	72	0.092784
	Total = 10	Total = 493		Total = 1,170	0.30 ± 0.13
(mean ± SD)					

Table 3 – The number of defined SWR events

The table summarizes the statistics of putative CA1 regions and SWRs. Only the first two sessions (sessions 1 and 2) from each subject were utilized to reduce the sampling bias.

Figures

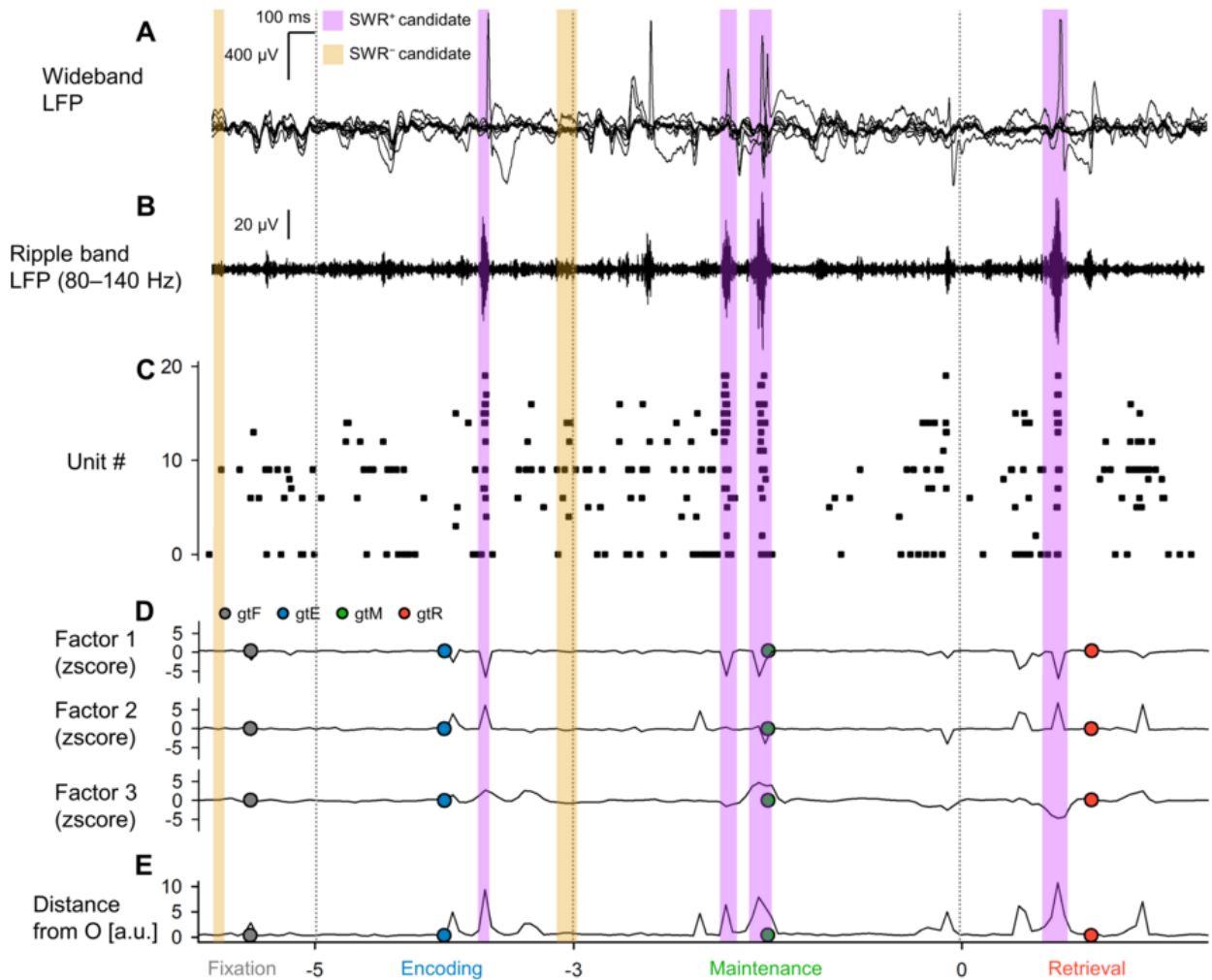


Figure 1 – Local field potential (LFP), multiunit activity, and neural trajectory of the hippocampus during a modified Sternberg task

A. Wideband LFP Trace: Displaying the intracranial encephalogram (iEEG) data for subject #6, session #2, trial #5, located in the left hippocampal head. This trace showcases the varying phases of the modified Sternberg working memory task, including fixation (gray, 1 s), encoding (blue, 2 s), maintenance (green, 3 s), and retrieval (red, 2 s). **B.** Ripple Band LFP: This presents the LFP trace in the ripple frequency band from the same trial and session. **C.** Multiunit Spike Raster: A plot illustrating multiunit spikes recorded during the mentioned trial. **D.** Neural Trajectory Factors: Depicting the first three factors of the hippocampal trajectory for the trial, determined by Gaussian-process factor analysis on spike counts with 50-ms bins. The dot circles signify the geometric median coordinates for each of the four task phases. **E.** Trajectory Distance Analysis: Shows the distance of the initial three trajectory factors from the origin (*O*). Note that highlighted rectangles overlaying the figure indicate the timings for SWR⁺ candidates (in purple) and SWR[−] candidates (in yellow).

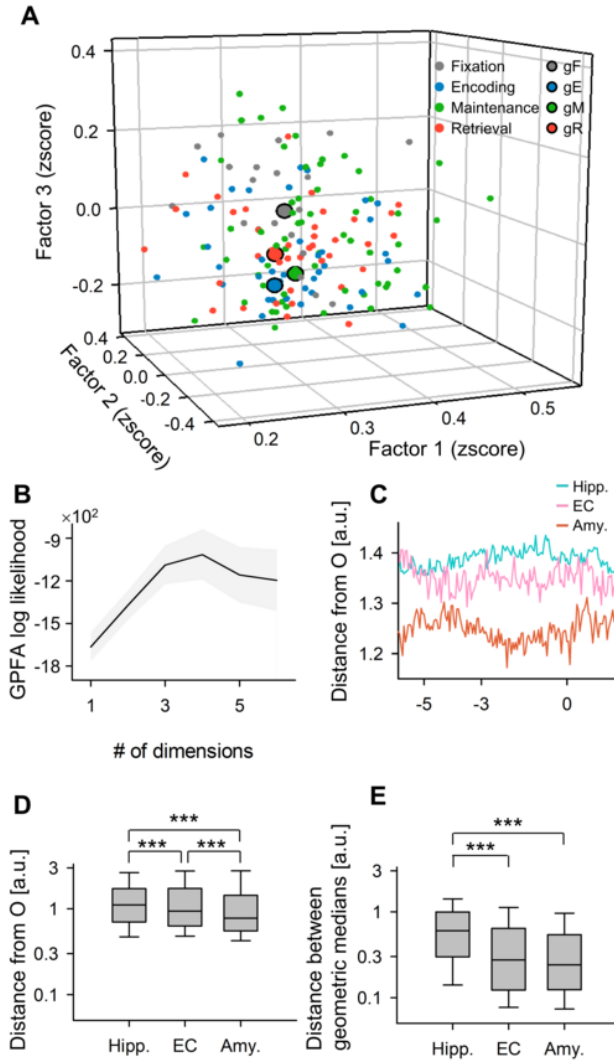


Figure 2 – State-dependent hippocampal neural trajectory

A. Neural Trajectory Visualization: This three-dimensional plot represents the neural trajectory of the left hippocampus derived from the Gaussian-process factor analysis (GPFA). Smaller points indicate coordinates of 50-ms neural trajectory bins within a session (median of 50 trials). Larger points with *black* edges represent geometric medians for each phase of the Sternberg working memory task, distinguished by colors for fixation (*gray*), encoding (*blue*), maintenance (*green*), and retrieval (*red*). **B.** GPFA Model Log-likelihoods: The graph showcases the log-likelihood predictions of GPFA models concerning the number of dimensions. Notably, the optimal dimension was identified as three using the elbow method. **C.** Distance Analysis from Origin: The plot represents the trajectory distance from the origin (*O*) for the hippocampus (Hipp.), entorhinal cortex (EC), and amygdala (Amy.), plotted against the time since probe onset. **D.** Trajectory Distance in Medial Temporal Regions: The box plots display the trajectory distances from *O* for each region, with the hippocampus showing the greatest distance, followed by the EC and the Amygdala. **E.** Inter-phase Trajectory Distances: This visualizes the distance variations between trial trajectory geometric medians of task phases. The distances in the hippocampus were observed to be more pronounced compared to the EC or Amygdala.

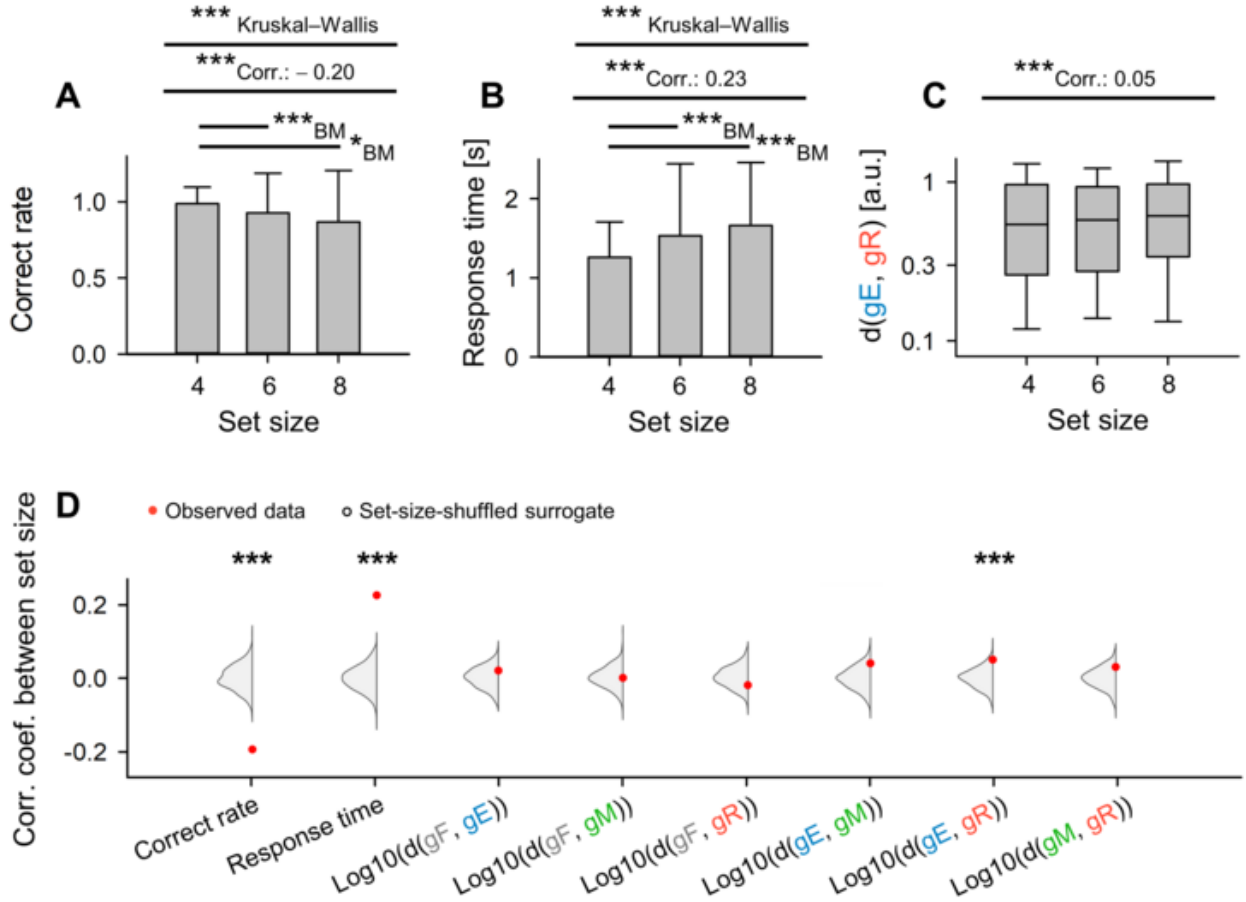


Figure 3 – Influence of memory load on encoding and retrieval states in the hippocampus

A. Relationship between set size (number of letters encoded) and correct rate in the WM task. Notably, a negative correlation was observed (coefficient = -0.20 , $***p < 0.001$), analyzed using set-size-shuffled surrogate. Significance was determined using Kruskal–Wallis test, followed by the Brunner–Munzel test with Bonferroni correction. **B.** Association between set size and response time post-probe initiation. A positive correlation was detected (coefficient = 0.23 , $***p < 0.001$), analyzed using set-size-shuffled surrogate. Statistical tests included the Kruskal–Wallis and post-hoc Brunner–Munzel tests with Bonferroni correction. **C.** Analysis of set size against the distance between geometric medians during encoding and retrieval phases (represented as $\|g_E g_R\|$). A correlation of 0.05 was noted for set size and $\log_{10}\|g_E g_R\|$, analyzed using set-size-shuffled surrogate. **D.** Experimentally observed correlations between set size and various parameters are illustrated by *red* dots. The *gray* violin plots contrast these findings with set-size-shuffled surrogate data ($n = 1,000$), emphasizing the significant observed correlation coefficients ($***p < 0.001$). Abbreviations: g_F , g_E , g_M , g_R represent the geometric median of trajectories during fixation, encoding, maintenance, and retrieval phases, respectively.



Figure 4 – SWR detection in putative CA1 regions

A. Two-dimensional UMAP (uniform manifold approximation and projection)[41] representation of unit activities during SWR⁺ candidates (*purple*; potential SWR events) and SWR⁻ candidates (*yellow*; controls for SWR⁺ candidates). **B.** Cumulative density plot illustrating silhouette scores for different hippocampal regions (refer to Table 2). Regions with silhouette scores exceeding 0.60 (75th percentile) are considered as putative CA1 regions. Within these regions, SWR⁺ and SWR⁻ candidates are identified and categorized as SWR⁺ ($n = 1,170$) and SWR⁻ ($n = 1,170$), respectively. **C.** Overlapping duration distributions [ms] for SWR⁺ (*purple*; 93.0 [65.4], median [IQR]) and SWR⁻ (*yellow*; 93.0 [65.4], median [IQR]). The identical overlap results from their definition criteria. **D.** Depiction of ripple incidence [Hz] for both SWR⁺ (*purple*) and SWR⁻ (*yellow*) relative to time from the probe, represented as mean \pm 95% confidence interval. However, the 95% confidence interval might not be readily discernible due to its narrow range. Note the significant elevation in SWR incidence between 0–400 ms post-probe, surpassing the 95th percentile of bootstrap samples (0.421 [Hz], $*p < 0.05$). **E.** Histogram showcasing ripple band peak amplitude distributions for SWR⁻ (*yellow*; 2.37 [0.33], median [IQR]) versus SWR⁺ (*purple*; 3.05 [0.85], median [IQR]). A notable difference is present between the two, confirmed with $***p < 0.001$ using the Brunner–Munzel test.



Figure 5 – Transient neural trajectory change during SWR

A. Distance from the origin (*O*) of the peri-sharp-wave-ripple trajectory (mean \pm 95% confidence interval; however, the interval may not be easily visible due to the narrow range.). **B.** The distance from the origin during the mid-SWR⁺ period was found to be longer compared to the corresponding pre-SWR⁺ period (* p < 0.05, ** p < 0.01, *** p < 0.001; Brunner–Munzel test). Abbreviations: SWR, sharp-wave ripple events; eSWR, SWR during the encoding phase; rSWR, SWR during the retrieval phase, SWR⁺, SWR event; SWR⁻ control events for SWR⁺; pre-SWR, mid-SWR, or post-SWR, the time interval from -800 to -250 ms, from -250 to +250 ms, or from +250 to +800 ms from the center of SWR.

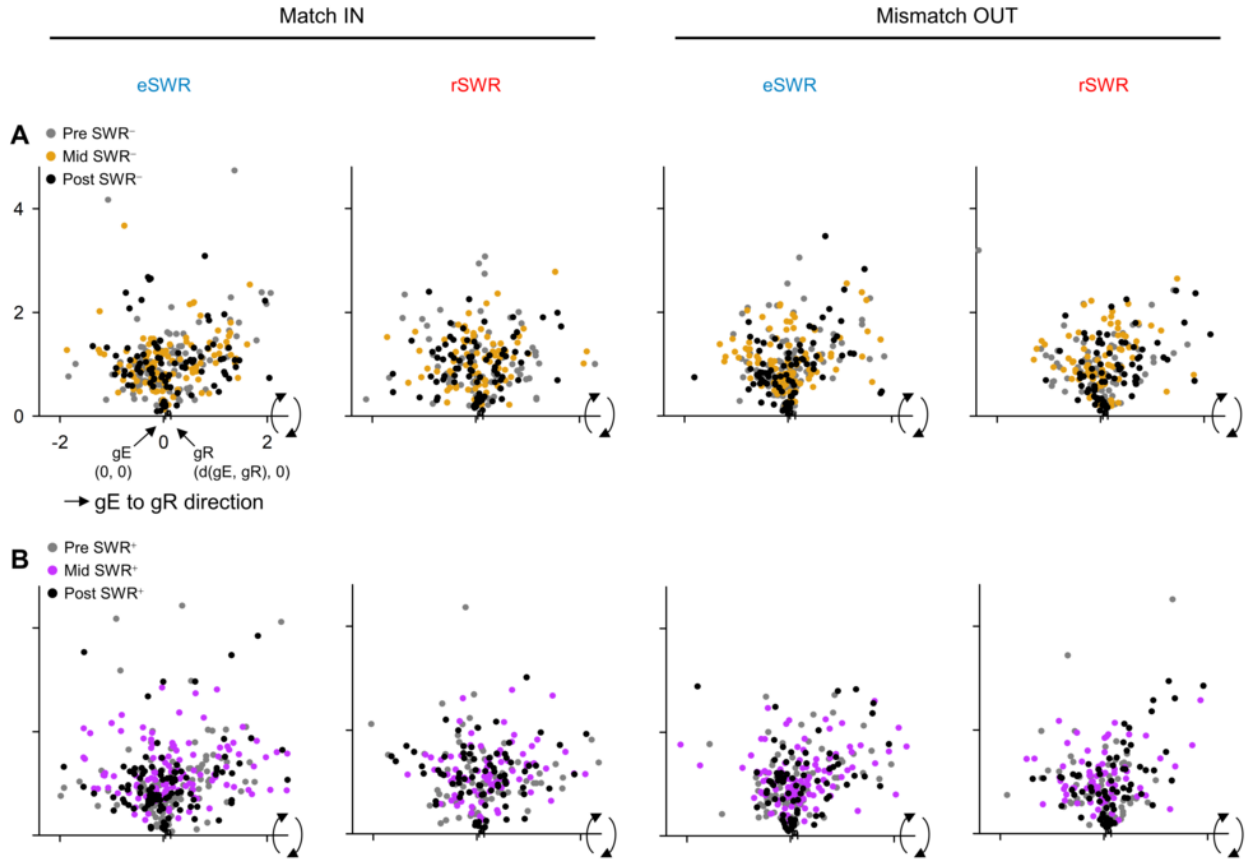


Figure 6 – Coordinates of neural trajectory during sharp-wave ripple aligned by encoding and retrieval states.

A. Hippocampal neural trajectories during pre- (gray), mid- (yellow), and post-SWR⁻ (black) in Match IN (left) and Mismatch OUT task (right). **B.** The equivalents for SWR⁺ instead of SWR⁻, though mid-SWR⁺ is depicted with purple. All data points underwent adjustments and rotations to fit a two-dimensional representation, positioning g_E at (0, 0) and g_R at ($\|g_E g_R\|$, 0). The $\|g_E g_R\|$ metric varies across sessions, and its median \pm IQR (with medians approximately 0.2) is presented on the x-axes. Note: some intervals might be challenging to discern because of their narrow range. In this two-dimensional depiction, both the distances and angles preserve their relationships as in the original three-dimensional space. Abbreviations: SWR, sharp-wave ripple events; eSWR, SWR during the encoding phase; rSWR, SWR during the retrieval phase; SWR⁺, SWR event; SWR⁻ control events for SWR⁺; pre-SWR, mid-SWR, or post-SWR, the time interval from -800 to -250 ms, from -250 to +250 ms, or from +250 to +800 ms from the center of SWR.

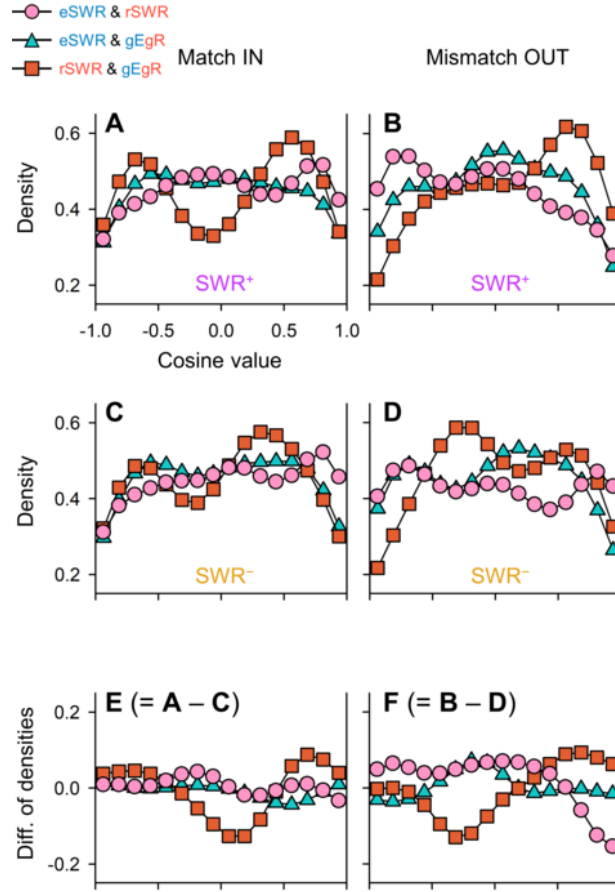


Figure 7 – Analysis of Neural Trajectory Directions during SWR between Encoding, and Retrieval States.

A–B Kernel density estimation (KDE) distribution of $\overrightarrow{eSWR^+} \cdot \overrightarrow{rSWR^+}$ (pink circles), $\overrightarrow{eSWR^+} \cdot \overrightarrow{gEgR}$ (blue triangles), and $\overrightarrow{rSWR^+} \cdot \overrightarrow{gEgR}$ (red rectangles) in Match In (**A**) and Mismatch OUT task (**B**). **C–D**. The corresponding distributions of SWR^- in response to those of SWR^+ in **A–B**. **E–F**. The differences in distributions, highlighting the SWR components (**E** = **C** – **A**; **F** = **B** – **D**). Note the inverse directionality between $\overrightarrow{eSWR^+}$ and $\overrightarrow{rSWR^+}$ only in Mismatch OUT task (pink circles in **E–F**). Additionally, the shifts from the retrieval to encoding states were observed for SWR components both in Match IN and Mismatch OUT tasks (red rectangles in **E–F**).